J. Fluid Mech. (1994), *vol.* 259, *pp.* 305–331

Emergence and evolution of triangular vortices

By G. F. CARNEVALE[1] AND R. C. KLOOSTERZIEL[2]

[1] Scripps Institution of Oceanography, University of California, San Diego, La Jolla, CA 92093, USA

[2] School of Ocean & Earth Science & Technology, University of Hawaii, Honolulu, HI 96822, USA

(Received 23 September 1992 and in revised form 26 July 1993)

Laboratory observations and numerical simulations reveal that, in addition to monopoles, dipoles and tripoles, yet another stable coherent vortex may emerge from unstable isolated circular vortices. This new vortex is the finite-amplitude result of the growth of an azimuthal wavenumber-3 perturbation. It consists of a triangular core of single-signed vorticity surrounded by three semicircular satellites of oppositely signed vorticity. The stability of this triangular vortex is analysed through a series of high-resolution numerical simulations and by an investigation of point-vortex models. This new compound vortex rotates about its centre and is stable to small perturbations. If perturbed strongly enough, it undergoes an instability in which two of the outer satellites merge, resulting in the formation of an axisymmetric tripole, which subsequently breaks down into either a pair of dipoles or a dipole plus a monopole. The growth of higher-azimuthal-wavenumber perturbations leads to the formation of more intricate compound vortices with cores in the shape of squares, pentagons, etc. However, numerical simulations show that these vortices are unstable, which agrees with results from point-vortex models.

1. Introduction

In the realm of two-dimensional fluid dynamics, several types of stable coherent vortices are known. Firstly, we have the circularly symmetric vortex with single-signed monotonic vorticity profile (a 'monopole') and, secondly, the self-propelling dipole, consisting of two closely packed counter-rotating vortices. In addition to these classical cases, in recent years another non-trivial stable coherent vortex has been found and dubbed the tripole (see Legras, Santangelo & Benzi 1988; van Heijst & Kloosterziel 1989). The tripole consists of a linear arrangement of three regions of distributed vorticity of alternate signs, and the axis of this configuration rotates about the centre of the core vortex. Laboratory observations (Kloosterziel & van Heijst 1991; van Heijst, Kloosterziel & Williams 1991) and numerical simulations (Legras *et al.* 1988; Carton, Flierl & Polvani 1989; Carton & McWilliams 1989) show that the tripole is the finite-amplitude result of the growth of a wavenumber-2 perturbation on an unstable, isolated circular vortex. The wavenumber m is defined as usual with the angular dependence of the perturbation in polar coordinates (r, θ) proportional to $\exp(im\theta)$. Laboratory observations (Kloosterziel 1990), normal-modes analysis (Gent & McWilliams 1986) and analysis of simple model vortices (Flierl 1988) indicate that which azimuthal wavenumber grows fastest depends on the steepness of the initial velocity profile.

Since laboratory and numerical observations revealed the existence of tripoles as a

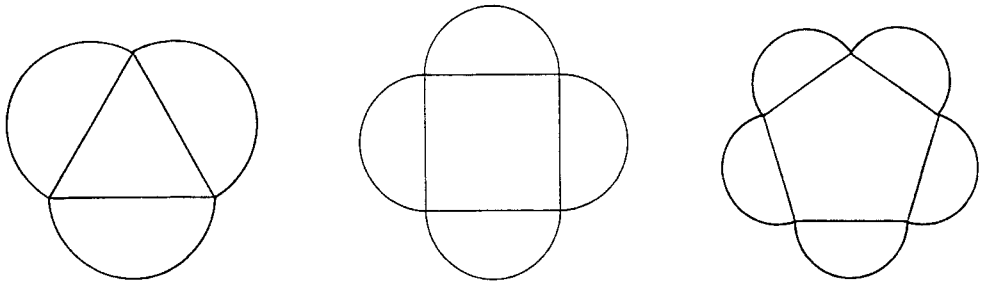

FIGURE 1. Diagram showing idealized forms of the first three members of a family of geometrical vortices. In each case, the core vortex is in the shape of a regular polygon of n sides and the core is surrounded by n semicircular satellites with vorticity of opposite sign. Cases corresponding to $n = 3$, 4 and 5 are shown here.

result of the finite-amplitude equilibration of a wavenumber-2 mode, it was natural to search for higher-order instabilities that might lead to other, even more intricate coherent vortices. We report on the finite-amplitude form of wavenumber 3 and higher wavenumber instabilities on isolated circular vortices, and the stability of the resulting compound vortices. The nonlinearly saturated states that result from these instabilities have a central core of vorticity of one sign with a boundary approximately in the shape of a regular polygon of n sides. This boundary is maintained by the interaction between the core and n semicircular satellites of oppositely signed vorticity. The first three members of this family are depicted schematically in figure 1, and for simplicity we will call them by the geometrical structure of their cores. In all cases, these compound vortices instantaneously rotate about the centre of the core. We demonstrate that, of this class of vortices, it is very likely that only the triangle vortex is stable. As with the dipole and tripole, an analytic proof of stability of the triangle vortex is lacking, and we must have recourse to numerical simulation and models to indicate stability to finite-sized perturbations. Of all the stable compound vortices, the triangle is the least robust, and perhaps we should talk of marginal stability here since it is unstable to rather small perturbations. In any case, understanding that stability has not yet been proven analytically for any of the compound vortices, it appears that the dipole, tripole, and triangle vortex may form the complete set of stable compound vortices of zero circulation.

In §2 we provide experimental evidence that, under certain conditions, an isolated circular laboratory vortex shows the rapid growth of a wavenumber-3 instability. At finite amplitude this leads to the formation of the triangular vortex as schematically depicted in figure 1. The resulting triangular laboratory vortex is usually unstable and two of the satellites are observed to merge, thus shortly yielding a tripolar form, which subsequently breaks up into two dipoles or a dipole and a monopole. These laboratory observations inspired the numerical study discussed in §3. It is shown there that a *stable* triangular vortex forms if the vortex is initially seeded with a pure wavenumber-3 perturbation. A linear stability analysis is presented which explains the variability of results in the laboratory as a competition between unstable modes of different wavenumbers. Another stability analysis, presented in §3, uses finite-amplitude perturbations in high-resolution simulations to show that the symmetrical triangular vortex is stable if the initial perturbations are sufficiently small.

In §4, we analyse the behaviour of the geometrical vortices by using point-vortex models. In such a model each of the regions of single-signed vorticity is replaced by an equivalent point vortex of the same circulation as that of the given region. The

triangular vortex is thus modelled by a central point vortex surrounded by three point vortices of opposite circulation. We find that the first stage of the observed instability, i.e. the close approach of two of the satellites, is intrinsic to the model when the positions and/or strengths of the satellites are sufficiently perturbed from their equilibrium positions and values. Finally, following a study by Morikawa & Swenson (1971), the point-vortex models for the higher-order compound vortices are considered. These are found to agree with the numerical simulations for the square and pentagon vortices which are unstable.

2. Laboratory experiments

A number of experiments have been performed in a rotating cylindrical tank, 125 cm in diameter and 50 cm deep, placed on a large rotating table. The rotating tank is filled with water and brought to solid-body rotation, with a bottomless cylinder placed concentrically in the tank. Vortices were created by briefly stirring the fluid confined to the inner cylinder which, after the stirring-induced motion becomes purely azimuthal, was lifted vertically. Photographs of passive scalar (dye) were taken with a camera mounted in the rotating frame above the free surface of the fluid. The working depth of the fluid was 11 cm and the rotation period of the tank $T = 9$ s. The diameter of the cylinder was 10 cm. With this stirring method we have very little control over the details of the initial velocity profile. However, the wavenumber-3 instability could easily be observed in the following manner. In the inner cylinder, we create an *anticyclone* which away from the boundary layer at the wall of the cylinder is close to solid-body rotation (this profile is easily set up by stirring smoothly close to the wall). The Rossby number of these vortices is not small (i.e. $O(1)$ or larger) and they are therefore, as discussed by Kloosterziel & van Heijst (1991), centrifugally unstable when released in the ambient fluid. When the inner cylinder is lifted vertically, vigorous vertical and horizontal mixing occurs at the rim of the vortex. This results in an azimuthal velocity profile which is unstable to wavenumber-3 perturbations. Rotation tends to make fluid motions two-dimensional with vertical motions disappearing within a few rotation periods of the tank through radiation by inertial waves (Greenspan 1968). Even before all vertical motion has been subdued, the growth of the azimuthal mode can become apparent and a triangular vortex forms. It should be noted that in the case of a similarly created *cyclone*, no centrifugal mixing occurs and the vortex does not show the growth of a wavenumber-3 instability. The role of the centrifugal mixing is important only in so far as it helps set up an initial vorticity distribution that is susceptible to this two-dimensional instability.

In the laboratory experiments, the triangle vortices always broke down within one rotation period of the vortex. A typical sequence of events is shown in figure 2. The flows were visualized by adding dye to the fluid in the inner cylinder before it was withdrawn. A set of streakline photographs showing a similar sequence of events was previously presented by Kloosterziel & van Heijst (1991). The photograph in figure 2(*a*) was taken shortly after the cylinder was lifted. The fuzziness of the dye is an indication of the vertical and horizontal mixing that occurs and the growth of a wavenumber-3 perturbation is already clearly discernible. In figure 2(*b*), the formation of the three satellites is clearly visible. The structure has rotated more than 90° clockwise with respect to (*a*). The upper left satellite is somewhat underexposed in this picture. In figure 2(*d*) we see that this satellite moves towards the neighbouring satellite (in a clockwise direction) and subsequently in figures 2(*e*) and 2(*f*) we observe that it moves between that neighbouring satellite and the core, while the core simultaneously

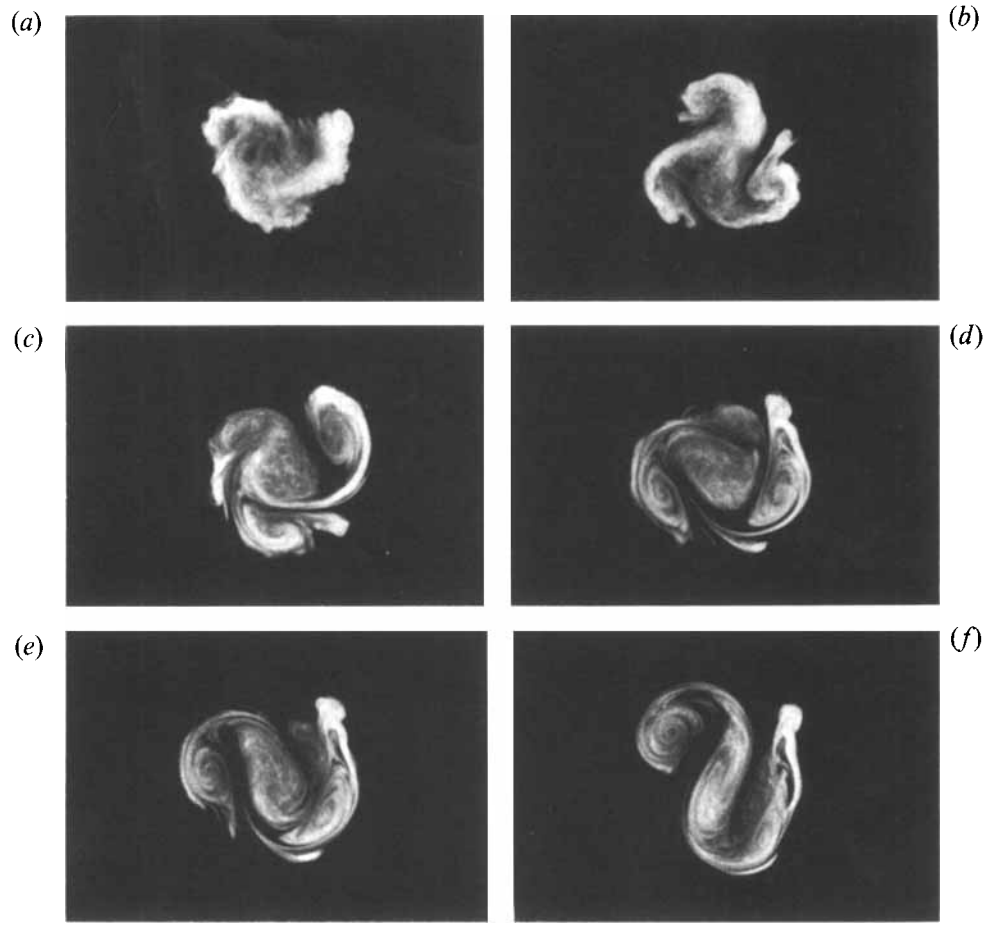

FIGURE 2(*a–f*). For caption see facing page.

loses its triangular shape. In figure 2(*f*) we observe an almost symmetric pattern with one lobe (upper left) consisting of one of the original satellites and the other lobe (lower right) consisting of the two tightly packed satellites which are in the process of merging. In figure 2(*g–i*) the two merging satellites can still be discerned. While the merger is in progress, the cyclonic vortices shear the central vortex into an elongated form. In figure 2(*i, j*) we see the anticyclonic core split in two parts, which in figure 2(*k, l*) roll up and collect each at the side of the cyclones. Thus two dipoles form and move away from each other in opposite directions. Another scenario that is sometimes observed is that after the merger the entire anticyclonic core pairs with the double cyclonic part to form one dipole, leaving behind a single cyclone. In any case, we always observe the merger of two satellites and a subsequent break up into either two dipoles or one dipole and a monopole.

Although we have tried to modify our experimental procedures, we have not been able to produce a triangle vortex which simply decays in amplitude while preserving its form. We tried to create a finite-amplitude pure mode-3 instability by deforming the confining cylinder with three symmetrically spaced indentations. This procedure resulted in a more symmetric triangle vortex. The typical dye pattern that forms is shown in figure 3. Clearly visible are the triangularly shaped core and the three

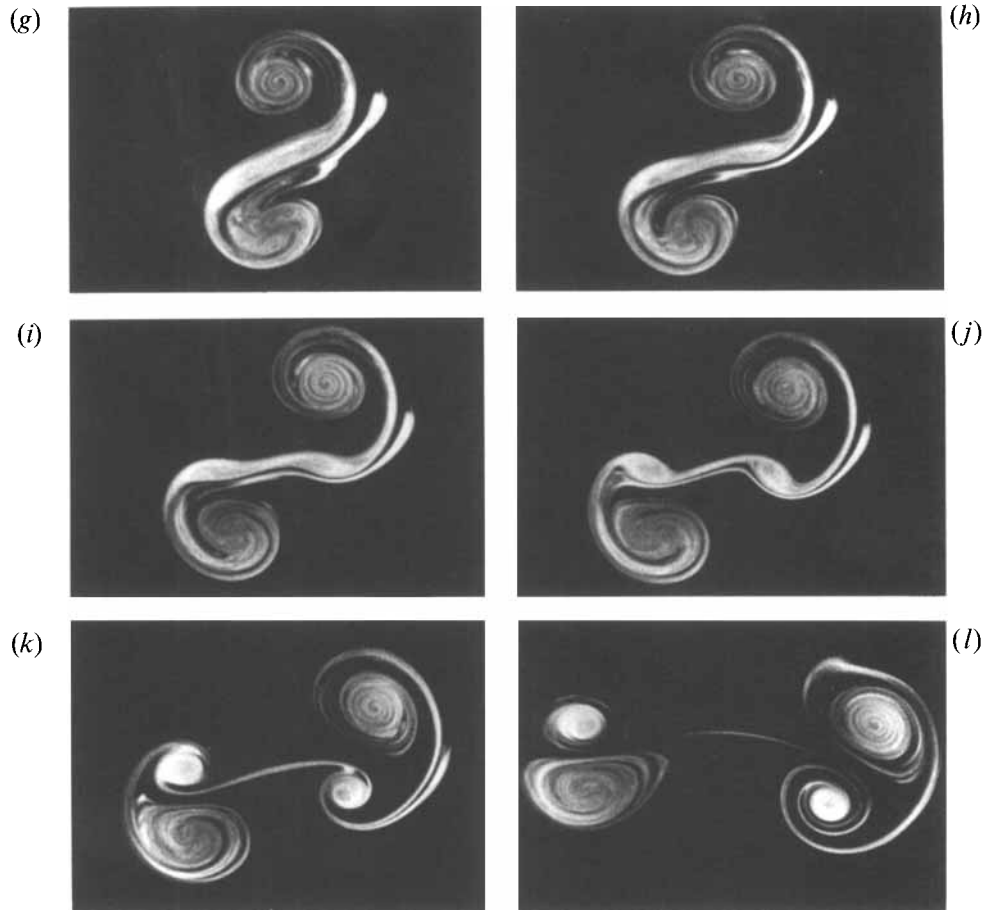

FIGURE 2. Plan-view photographs showing the characteristic evolution of a triangular vortex in a rotating fluid. The experiment was carried out in a large (125 cm diameter) tank placed on a turntable. The working depth of the fluid was 11 cm and the horizontal scale of the photographs is 80 cm. Increasing time is from left to right, top to bottom. The photographs were taken in the rotating frame at times (*a*) $t = 0.0T$, (*b*) $2.2T$, (*c*) $8.9T$, (*d*) $11.1T$, (*e*) $12.2T$, (*f*) $13.3T$, (*g*) $15.6T$, (*h*) $16.7T$, (*i*) $17.8T$, (*j*) $18.9T$, (*k*) $20.0T$, (*l*) $23.3T$, where $T = 9$ s is the rotation period of the turntable. The evolution is visualized by adding dye to the vortex. The triangle vortex that forms rotates in a clockwise sense. The phases of the evolution are discussed in the text.

satellites, each resembling one half of a circle. The smaller-scale structures at the edge vary among the experiments. The flow is anticyclonic in the triangular core (clockwise) whereas the motion in the satellites is cyclonic. The whole structure rotates slowly in an anticyclonic sense. Although this vortex survives longer than that shown in figure 2, it also eventually broke down through merger of two of the satellites. In the next section, we examine the reason why it is so difficult to produce a truly long-lived triangle in these experiments.

With streakline photographs of particles floating on the free surface we can, as described in van Heijst *et al.* (1991), measure the vorticity distribution and streamfunction of such a vortex. From photographic records streaklines are digitized. By dividing the length of these streaklines by the exposure time of the photograph, one obtains a local velocity vector. We subsequently use an interpolation algorithm, on a 30×30 grid (described in some detail by Nguyen Duc & Sommeria 1988) to obtain an

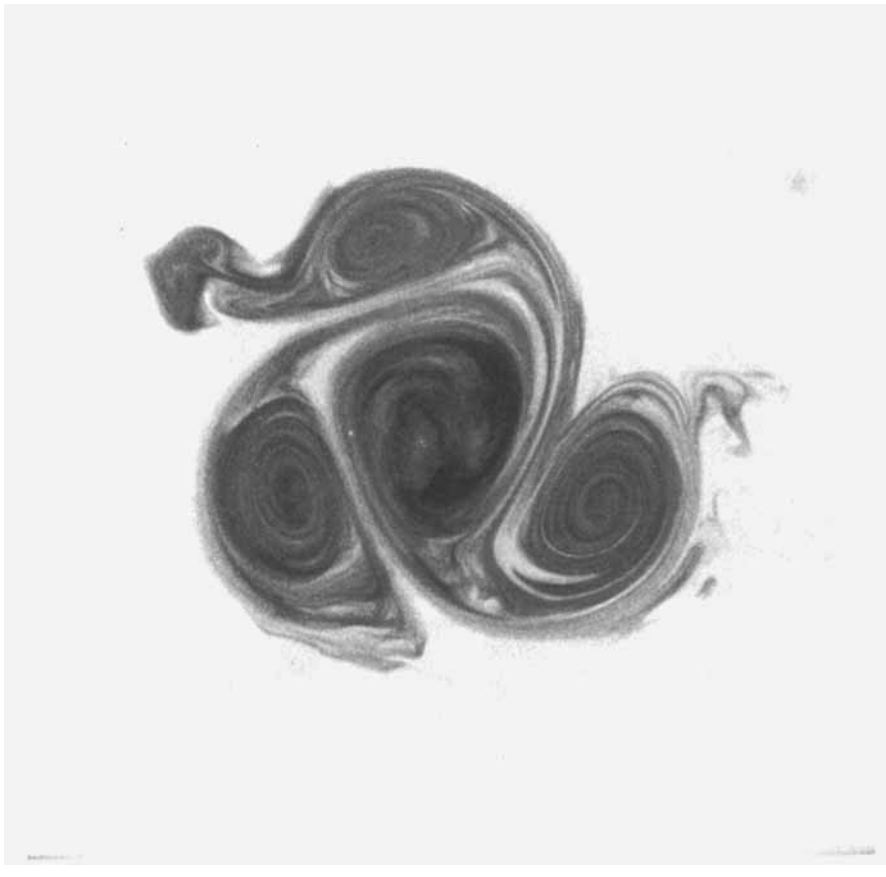

FIGURE 3. Photograph of the triangle vortex visualized by dye. This vortex was produced in the rotating-tank by stirring the water in a hollow cylinder with three equally spaced vertical indentations and then removing the cylinder vertically.

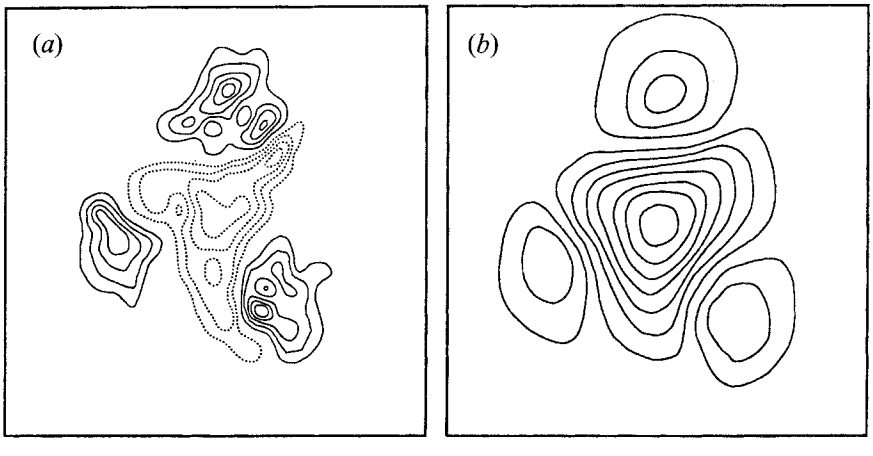

FIGURE 4. Graphs showing contours of (*a*) vorticity and (*b*) streamfunction of a laboratory triangular vortex (Kloosterziel 1990). In order to obtain these graphs, a streaklike photograph was digitized and the velocity field was subsequently derived from this. The vorticity field is calculated by differentiation of the velocity field. In (*a*), dashed (continuous) lines indicate negative (positive) vorticity values on equally spaced contour levels. The streamfunction is obtained by integration over the vorticity field.

interpolated velocity field. By differentiation one subsequently obtains an interpolated vorticity field and by integration the streamfunction. For a smooth interpolation, a digitized flow field best with a homogeneous spatial distribution of vector is best. Any clustering or local sparseness should be avoided because this may lead locally to unphysically large gradients and thus affect the vorticity distribution that is derived from the interpolated field. A characteristic example of contours of vorticity and the streamfunction of a triangular vortex is shown in figure 4. The irregular features in the vorticity distribution in (*a*) are due to there being few streaklines in certain areas, and small errors made in the measurement of the length and direction of the streaklines. However, a clear indication of the vorticity distribution is provided by this graph. All positive vorticity is confined to the three satellites whereas all negative vorticity is found in the core region. The features of the streamfunction in figure 4(*b*) are much smoother because it is obtained by integration of the vorticity distribution.

3. Numerical simulations

The laboratory experiments discussed above raise several questions. For one thing, we need to understand the circumstances under which triangle vortices arise. Furthermore, we question the longevity of the triangle vortex: why does it appear only as a transient state in the laboratory and are there conditions for which it would be long-lived? We have investigated these and related questions by using numerical simulations.

The simulations which we performed are for a purely two-dimensional flow. The precise form of the vorticity equation that we used is

$$\frac{\partial \zeta}{\partial t} + \boldsymbol{v} \cdot \boldsymbol{\nabla} \zeta = -\nu_0 \zeta + \nu_2 \nabla^2 \zeta - \nu_4 \nabla^4 \zeta, \tag{1}$$

where ζ is the relative vorticity, and $\boldsymbol{v}$ is the divergence-free velocity field, which is related to the streamfunction ψ according to

$$\boldsymbol{v} = (u, v) = \left(-\frac{\partial \psi}{\partial y}, \frac{\partial \psi}{\partial x} \right).$$

The dissipative terms on the right-hand side of (1) can be used to simulate various effects as needed. The first term, a Rayleigh friction, can be used to simulate the effect of the Ekman damping by the lower Ekman layer in the rotating-tank experiments. In that case, $\nu_0 = 1/T_E$, where the Ekman decay time is given by $T_E = D/(\nu\Omega)^{\frac{1}{2}}$, with ν the molecular kinematic viscosity of water ≈ 0.01 cm^2 s^{-1}, D the depth of the water, and Ω the tank rotation period. In the cases simulating the rotating-tank environment, we set $\nu_2 = \nu$. The final term, referred to as the hyperviscosity, is very useful in simulating an 'inviscid' flow in a finite-resolution simulation. In that case, we set $\nu_0 = \nu_2 = 0$ and give ν_4 the smallest possible value that will prevent build-up of small-scale enstrophy due to the finite resolution while keeping energy decay at negligible levels. The method of simulation used is the spectral method of Patterson & Orszag (1972) on a doubly periodic domain of $N \times N$ grid points. We employed an isotropic spectral truncation at wavenumber $k_{trunc} = (8/9)^{\frac{1}{2}} N$. We will report the resolutions used in these simulations in terms of the equivalent number of grid points on the spatial grid where this implies a spectral representation involving all wavevectors of magnitude less than k_{trunc}. Unless indicated otherwise, the results reported were obtained at resolution 128×128. To make sure that inaccuracies due to resolution were not significant, many checks

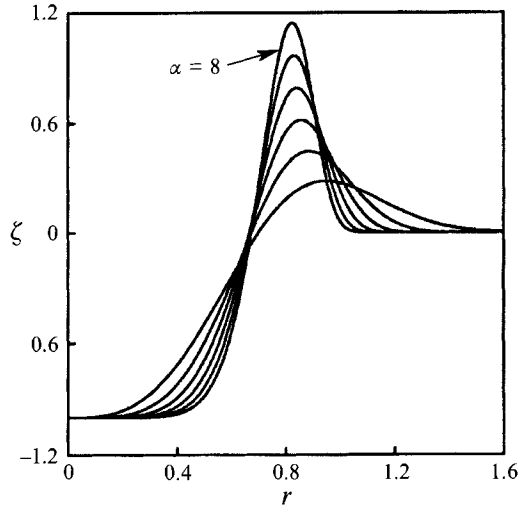

FIGURE 5. Plot showing the radial vorticity profile for the unperturbed vorticity distribution defined in equation (2). The curves correspond to values of the steepness parameter $\alpha = 3, 4, 5, 6, 7$ and 8. The larger values of α correspond to narrower annuli of positive vorticity, flatter distributions of vorticity in the core, and steeper slopes in the distribution between the negative and the positive annulus.

were performed by comparing the 128×128 simulations with 64×64 and 256×256 runs.

3.1. *Random initial perturbations*

We performed a series of simulations intended to capture the evolution of the flow in the rotating-tank experiments. For the initial conditions in these runs we use a nearly circularly symmetric vortex, with enough asymmetry to mimic the inevitable irregularities in the vortex generation in the tank. We start with a basic circularly symmetric state given in non-dimensional form by

$$\zeta = -(1 - \tfrac{1}{2}\alpha r^{\alpha})\,\mathrm{e}^{-r^{\alpha}}, \tag{2}$$

where r is the radial distance from the centre of the vortex. Distances have been non-dimensionalized by L, the horizontal lengthscale of the vortex, and velocities by U. This is the same profile used in several significant previous studies (e.g. Carton & McWilliams 1989). In figure 5 we show the radial structure of this unperturbed vortex for integer values of α from 3 to 8. Note that increasing α makes the vorticity in the core more uniform, the width of the annulus smaller, and the slope of the graph between the core and the annulus steeper. We will refer to α as the steepness parameter. This family of profiles is a reasonable model for the types of isolated vortices created in the tank.

Orlandi & van Heijst (1992) successfully simulated the generation and evolution of a triangle vortex similar to that shown in figure 2 by using an initial condition in which the basic state in (2), with $\alpha = 5$, is perturbed with a randomly generated vorticity field defined by

$$\zeta' = \eta \exp\left[\frac{(\alpha r^{\alpha} - 2)^2}{2\sigma^2}\right] - c. \tag{3}$$

Here $\eta(x, y)$ is a random number uniformly generated on the range $(-\eta_0, \eta_0)$ for each grid point, and c is a constant chosen to ensure that the spatially integrated value of

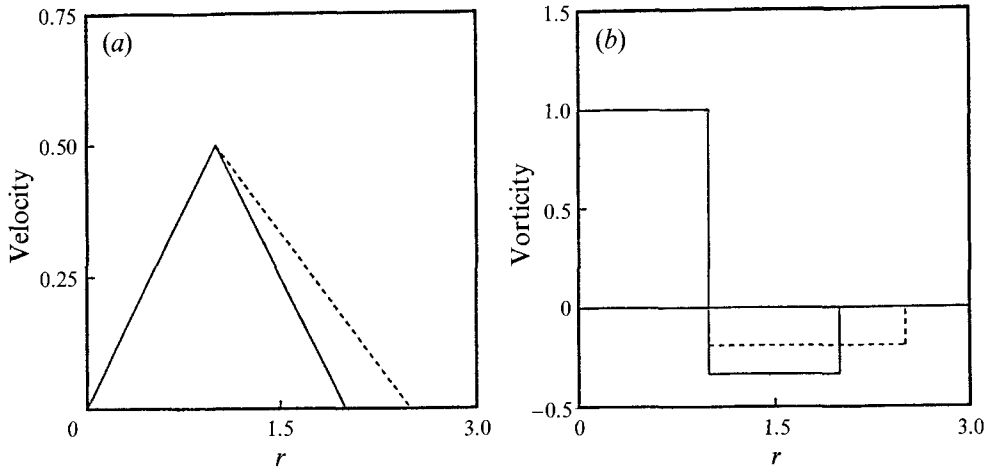

FIGURE 6. Diagram of the isolated model vortex investigated by Flierl (1988). In (*a*) the velocity profile is shown and in (*b*) the corresponding vorticity. Non-dimensionally the profiles have maximum velocity at $r = 1$ and zero velocity beyond $r = d$. If the velocity profile is steep enough (solid line), the vortex becomes linearly unstable, first to wavenumber-2 instabilities, while higher-wavenumber instabilities can have the fastest growth rate for even steeper velocity distributions.

ζ' (i.e. the circulation of the perturbation) vanishes. This perturbation is concentrated at the radius where the unperturbed vorticity field changes sign, and σ can be adjusted to make the perturbation penetrate the core and annulus to any desired degree. In our series of simulations, we varied α from 5 to 8 in integral increments, varied the strength of the perturbation η_0 between 0.1 and 1.0, and chose various seeds for the random-number generation.

The variety of behaviour in our simulations matched the variety observed in the tank experiments. Some cases went through a triangle vortex stage, while others formed just a tripole, which then broke down either into a pair of dipoles or a monopole plus dipole. Even for a fixed setting of α and η_0 these different scenarios can be obtained by changing the seed of the random number generator. We found our best examples of triangle formation for values of $\alpha = 6$ and 7.

3.2. *Linear stability analysis*

It is natural to ask why is there so much variation, in both laboratory experiments and numerical simulations. It seems, from the observations, that there is a competition between early tripole formation (wavenumber-2 instability) and triangle formation (wavenumber-3 instability) that is responsible for the variability. To pursue this hypothesis, we turn to linear stability analysis of the unperturbed profile in equation (2). Flierl (1988) examined analytically the linear stability of the two-patch vortex system shown here in figure 6. He found that as the relative width of the outer annulus is decreased the azimuthal modes become unstable in sequence beginning with mode 2. They consist of a circular core of constant vorticity $q_1 = 1$ between $r = 0$ and 1, surrounded by an annulus of oppositely signed constant vorticity $q_2 = -q$ between $r = 1$ and d (see figure 1). These are isolated vortices, i.e. the azimuthal velocity is zero for $r > d$. For large d (small q) these model vortices are linearly stable to perturbations with any wavenumber. For $d < 2$ $(q > \frac{1}{3})$, $m = 2$ perturbations are unstable, for $d < (1+\sqrt{2})^{\frac{1}{2}}$ $(q > 1/\sqrt{2})$, the $m = 3$ mode is unstable, and so on. The steeper the velocity profile (solid line in figure 6*a*), the higher the wavenumber of the fastest growing mode. By analogy, we can expect that, as the value of the steepness parameter

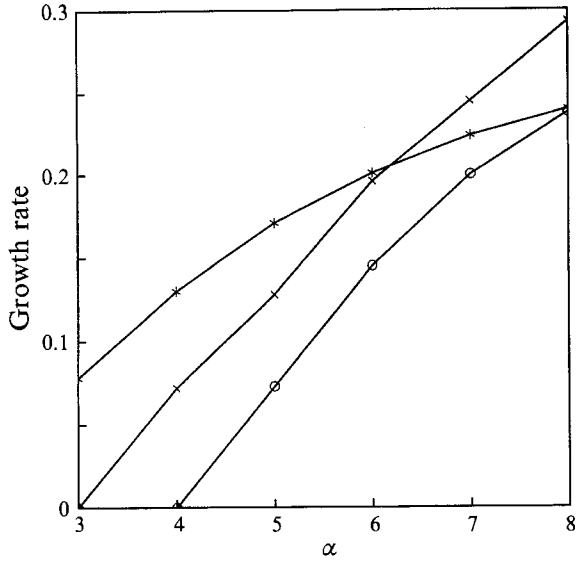

FIGURE 7. The non-dimensional growth rates for azimuthal modes 2 (*), 3 (+), and 4 (○), shown as functions of the steepness parameter α (see (2)).

α is increased, higher and higher azimuthal modes will be unstable for our continuous profile. In order to understand the observed competition between these modes, we need to examine the actual values of the growth rates involved. To measure these growth rates, we ran a linearized inviscid version of the simulation code. That is, we performed simulations of

$$\frac{\partial \zeta'}{\partial t} + \boldsymbol{v}_0 \cdot \nabla \zeta' + \boldsymbol{v}' \cdot \nabla \zeta_0 = 0, \tag{4}$$

where ζ_0 is the unperturbed field given by (2) and ζ' is the perturbation taken initially to be

$$\zeta' = \mu \cos(m\theta) \exp\left[\frac{(\alpha r^\alpha - 2)^2}{2\sigma^2}\right], \tag{5}$$

where μ is a constant amplitude. The velocity fields $\boldsymbol{v}_0$ and $\boldsymbol{v}'$ are derived directly from these vorticity fields by assuming periodic boundary conditions. Simulations of the linearized equations at resolution 64×64 were performed for various values of the mode number m and the steepness parameter α. Each case was run long enough to identify a fastest growing mode and measure its growth rate. The resulting set of growth rates is graphed in figure 7. The growth rates for wavenumber 2 with $2 \leqslant \alpha \leqslant 5$ were previously calculated by Carton & McWilliams (1989) through a normal-modes analysis, and we used a comparison with their results to check our procedure and found complete agreement. The results were further checked against the early evolution of fully nonlinear simulations for modes $m = 2, 3, 4$ in the case $\alpha = 7$. Good agreement was found for over three orders of magnitude of perturbation energy growth. The accuracy of our linearized results would be poorest for the steepest profile used, that is for $\alpha = 8$. Those results were checked against simulations at resolution 256×256 and found accurate to within 6%, which is sufficient for our purposes. From the graphs in figure 7, we see here that for $5 \leqslant \alpha \leqslant 8$ modes 2, 3 and 4 are all growing with growth rates of roughly the same magnitude. For states initialized with a random

perturbation, as in the laboratory experiments or the fully nonlinear simulations, all of these modes are excited. There is not a sufficiently large difference in timescale to ensure that the most unstable mode will dominate before nonlinear effects take over. We speculate that the early competition between these modes leads to the variety of observed scenarios in the laboratory.

3.3. *Formation of stable symmetrical triangular vortices*

Given the results of the linear stability analysis, we supposed that the full array of behaviour observed in the laboratory experiments and the random initial condition simulations could be understood as simply a matter of the growing azimuthal mode with the highest initial amplitude 'winning' the competition before nonlinear effects take over. Since the initial stages of the observations show tripole formation, which we associate with a mode-2 instability, and triangle formation, which we associate with mode-3 instability, we performed a series of simulations with a perturbation on our basic profile (2) that is just a linear superposition of these two modes. Specifically, we took

$$\zeta' = (\mu_2 \cos(2\theta) + \mu_3 \cos(3\theta)) \exp\left[\frac{(\alpha r^\alpha - 2)^2}{2\sigma^2}\right], \tag{6}$$

where $\alpha = 6$ and μ_3 was held fixed at 0.1 while μ_2 was varied from one simulation to the next. For μ_2/μ_3 in the range from 0.25 to 2.0, the evolution does indeed cover the range of observed initial stages from nearly symmetric triangle formation with breakdown after about one rotation, to no discernible triangle but strong tripole formation. These simulations were performed with the only dissipation being hyperviscosity as discussed above.

Of this series of simulations, the one with $\mu_2/\mu_3 = 0.5$ followed the evolutionary scenario of the rotating-tank experiment shown in figure 2 particularly well. In figure 8, we show the evolution of a passive scalar field that was also calculated in the simulation. Figure 8(*a*) shows the circularly symmetric 'dye' distribution. Figure 8(*b*) shows a well-formed triangle core surrounded by three semicircular cyclones which are somewhat asymmetric in position and shape. At this point, the triangle has already rotated by about a quarter of a turn from its orientation when it first clearly formed. The satellite furthest from the triangle core pulls a filament of material away from one vertex of the triangle. This also appears to be happening in the laboratory experiment (compare with figure 2*c*). Next, after about another quarter of a revolution, we see in figure 8(*c*) the beginning of the merger of two of the satellites. Also note the light coloured filament which is the core material that had been pulled out by the process initiated in (*b*). This filament is also visible in the remaining panels and is very similar to such a filament observed in the laboratory experiment (compare figure 2*d–l*). In the simulation, we find that this is an active filament in the sense that associated with it is a persistent filament of negative vorticity, which was also drawn off from the core triangle vortex. In figure 8(*e*), the satellite merger is nearly complete and the splitting of the central core has begun. Figure 8(*f*) shows the final dipole splitting, which is quite similar to that shown for the laboratory experiment (compare figure 2*l*).

The spiral structure of the dye field within the vortices is due to the fact that the initial passive scalar distribution differs from the vorticity field distribution. In order to capture this effect smoothly, we have had to resort to using a hyperdiffusivity. The usual Laplacian diffusivity with a physically realistic diffusivity constant, which is three orders of magnitude smaller than molecular viscosity, proved inadequate for keeping small-scale noise due to finite-resolution effects from making the spiral filaments

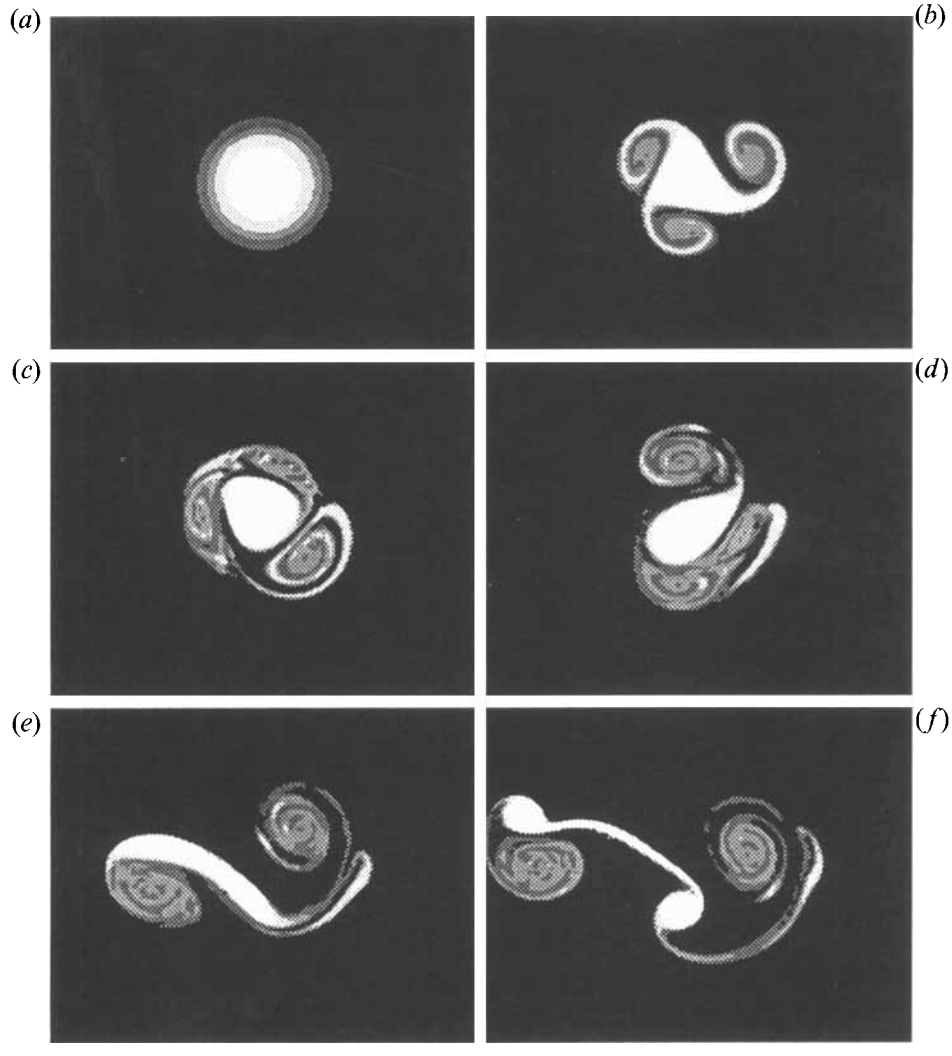

FIGURE 8. Shaded contour plot for the passive tracer field in a simulation of the evolution of a triangular vortex from a 5% mode-2 plus a 10% mode-3 perturbation on the circularly symmetric $\alpha = 6$ structure. The contour levels of the shaded regions are kept fixed from frame to frame (see text).

patchy on the scale of the widths of the filaments. We found that with a diffusivity of the form $\kappa_8 \nabla^8$ the coefficient κ_8 could be determined empirically so that it was small enough to allow formation of thin filaments but large enough to prevent undue breakup of these filaments. Simulations using only physical values for both diffusivity and viscosity show all the same features discussed in the previous paragraph. Besides the patchiness of the passive scalar spiral filaments and a change in timescale, the main difference with the viscous simulation has to do with the filament that was expelled from the core. In the inviscid case, the vorticity associated with this filament does not decay, while in the viscous case it decays by an order of magnitude in amplitude over the course of the run.

Continuing the series of inviscid simulations based on the perturbation (6) (with $\alpha = 6$), we found that for cases in which $\mu_2/\mu_3 < 0.25$ the triangle continued to rotate with no sign of breaking down. This was a surprise because in all of the laboratory experiments and simulations with random initial conditions, the triangle vortices broke

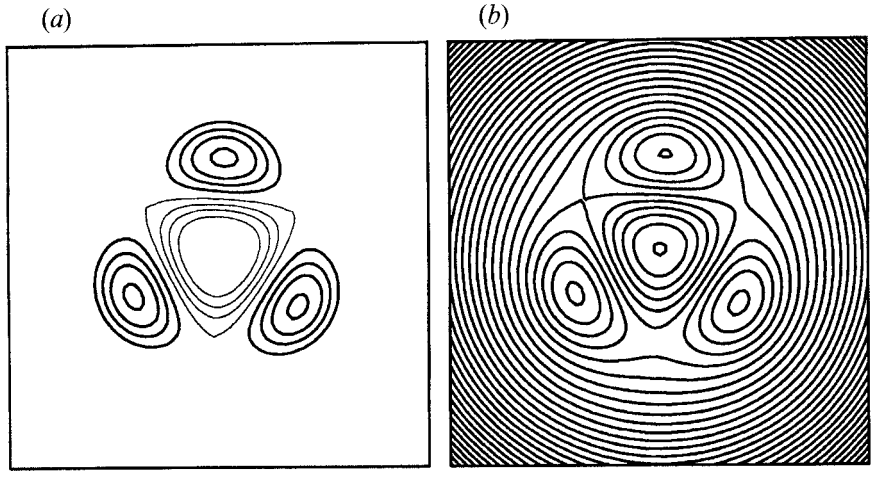

FIGURE 9. (*a*) Vorticity and (*b*) streamfunction contour plots of a numerically simulated triangular vortex. Thick (thin) contours in (*a*) indicate positive (negative) relative vorticity, and the contour level values are chosen to have increments of $\Delta\zeta = 0.2\ \mathrm{s}^{-1}$. The streamfunction, (*b*), is evaluated in the corotating frame with rotation period 81 s; the contour increment was taken as $\Delta\Psi = k^2\Delta\zeta$, where $k = j_1^1/a$ with $j_1^1 = 3.83$ and where $a = 12$ cm is approximately the radius of the semicircular satellites. The dimensional velocity and length scales used in the initialization were $U = 20$ cm/s and $L = 11$ cm, and the length of a side of the computational domain was 90 cm (although here we have only plotted the field over an inner square of 54 cm on a side).

down within one rotation period. Apparently, if modes other than mode 3 are sufficiently weak initially, a symmetric triangle vortex can form and persist. We performed several simulations with a pure mode-3 perturbation. In these simulations, we used various combinations of the values of the viscosity coefficient, ν_0, ν_2, and ν_4, to see if these choices had any appreciable effect on the form of the compound vortex that resulted. We found that there is no significant difference between the structures that form when we use, for example, viscosity, as appropriate to the rotating-tank experiments or no viscosity at all. In the latter case, however, small-scale noise appears.

In order to see if the emergence of a triangle that would persist in the laboratory environment is possible, we ran one case with a pure mode-3 initial perturbation and with viscosity appropriate to the rotating-tank conditions used in the experiment shown in figure 2. A fairly symmetric triangle forms by the end of the first rotation – it also takes about one rotation for the triangle to form in the purely inviscid case but the rotation period is about 15% shorter. Figure 9 shows the triangle structure in the viscous simulation after about two full rotations. It is not perfectly three-fold symmetric because of asymmetries associated with the finite resolution of the grid which have amplified during the evolution.

This triangle persisted unchanged in form although becoming somewhat broader in scale due to the effect of the Laplacian diffusion. During the course of the simulation the amplitude of the vorticity field decayed by three orders of magnitude and its energy by over six orders of magnitude under the influence of Ekman drag and molecular diffusion. This indicates that it should be possible to create a triangle vortex in the laboratory which would simply decay in amplitude.

Since the structure of the triangle vortex shown in figure 9(*a*) is typical of that observed even in the inviscid generation (save for the small-scale noise), we will explore it somewhat further here. In figure 9(*b*) we plot the streamfunction in the frame corotating with the triangle, that is, $\Psi = \psi - \frac{1}{2}\omega r^2$, where ω is the rotation rate of the

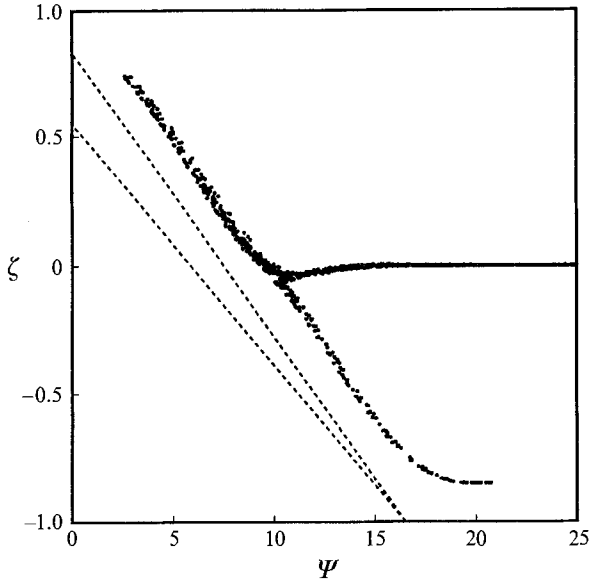

FIGURE 10. Scatter plot corresponding to the vorticity and streamfunction in the corotating frame shown in figure 9. The two dashed straight lines indicate the slope in the relationship which defines the internal structure of the Lamb dipole: $\zeta = (ka)^2 \Psi$, where $ka = j_1^1$ and where $a = 12 \pm 0.5$ cm give the limits on the measured radius of the semicircular satellites.

triangle, which we measured by allowing the vortex to rotate *inviscidly* for one revolution from the time of figure 9. With this estimate of the rotation rate, we computed the scatter plot of vorticity at each grid point versus the streamfunction in the frame corotating with the vortex. This is shown in figure 10. The spread of the points indicates that the state is not exactly stationary in the frame rotating with the estimated period, although it is nearly so. The horizontal branch corresponds to the exterior flow where the vorticity is negligible. The other branch has two sections. The part in the negative vorticity range comes from points in the triangular core. The part in the positive vorticity range comes from the satellites and is a roughly linear relationship. The combination of a linear relationship between Ψ and ζ and the semicircular structure of the boundaries suggests that the vorticity field in the satellites may be approximated by that of the celebrated Lamb dipole (Lamb 1932; Batchelor 1967). The vorticity field for this dipole is given by

$$\zeta = CJ_1(kr)\sin\theta \tag{7}$$

inside a circle of radius a and vanishes outside this circle. Here C is a constant and the parameter k is given by

$$ka = j_1^1 \approx 3.83, \tag{8}$$

where j_1^1 is the first zero of the J_1 Bessel function. In the case of the dipole, this solution corresponds to a linear relation between the streamfunction and vorticity field in the co-moving frame. If the satellites have a vorticity distribution given by (7), then the relation between Ψ and ζ, up to an arbitrary additive constant in Ψ, will be

$$\zeta = -k^2\Psi. \tag{9}$$

In view of (8), k can be determined by measuring the diameter of the satellites. From figure 9, we estimated the radius a to be 12 ± 0.5 cm. The two dashed lines in figure 10

have slopes that correspond to the estimated upper and lower limits on a. The steeper slope, corresponding to the lower limit, is a reasonable fit to the data. Also we note that, in accordance with our hypothesis, the contours in the satellites as shown in figure 9(a, b) nearly coincide when the ratio of the contour level increments is k^2. Thus it appears that the satellites are indeed quite close to half of a Lamb dipole. The analytic form for the interior solution is highly dependent on the vorticity distribution near the centre of the initial circular vortex.

3.4. *Stability of the triangular vortex*

We now turn to the question of why it is so difficult to produce a stable triangle vortex in the laboratory. We already know that viscosity is not responsible for the instability of the triangle vortex as shown by the simulations discussed above. Thus we now proceed to investigate the effects of perturbations to the symmetric triangle vortex. In these investigations we used the triangle state shown in figure 9 as the initial condition. We followed the inviscid evolution of this vortex for over twenty of its rotations without observing any evidence that it would break down. This was verified at both resolutions 64×64 and 128×128 (while at 256×256 the simulation was only checked for a few rotations due to the prohibitive expense of runs at that resolution). Although there was some variation of its form over that long period, the basic structure did not change significantly. Thus it appears possible that for inviscid flow the symmetric triangular vortex is a *stable* structure. The difficulty in finding a stable triangle vortex experimentally or in the corresponding random-perturbation simulations must be because it is only stable for perturbations with amplitude below some small threshold value.

To examine how large the tolerance for perturbations is, we performed two different kinds of stability tests. In the first, we perturbed the strength of the satellite vortices while leaving the inner triangle core unperturbed. This type of perturbation was suggested by an analysis of point-vortex models as discussed in the next section and by experience from the experiments and simulations discussed above. It seemed from these sources that the triangle may be very sensitive to variations in the strengths of the outer satellites which would lead to variations in the rate of revolution of the satellites about the core and thus permit a collision of a pair of satellites. The perturbation was prepared by taking the state shown in figure 9 and multiplying the vorticity field of the satellites by the factors $1+\delta$, $1-\delta$, 1, respectively, in one set of experiments, and by factors $1+\delta$, $1-\frac{1}{2}\delta$, $1-\frac{1}{2}\delta$, in a second series. All of the stability simulations were run with no bottom drag and no Laplacian viscosity; however, in order to avoid the build-up of enstrophy in the smallest scales during the long runs, hyperviscosity was used. In figure 11(a), we plot the time it takes until a merger occurs between two of the satellites in each of these series of experiments. The time is given in units of the rotation period of the unperturbed vortex and the simulations were terminated after 20 rotation periods even if no breakdown had occurred. For perturbations less than 2% the triangle remains intact for more than 20 rotation periods. There is a steep fall off of the time to merger or breakdown between perturbations of 2 and 4%. Defining a stability boundary based on simulations requires some arbitrary choice of how to define the stable regime since numerical noise will eventually contaminate the results. For practical purposes, we can take our stability boundary to be approximately where the lifetime, as a function of the perturbation amplitude, becomes very large. Thus in figure 11(a) the stability boundary is around 3%. This estimate can be compared to the rough estimates of the stability boundary for dipoles being about 10% judging from studies of dipoles propagating over topography (Carnevale *et al.* 1988).

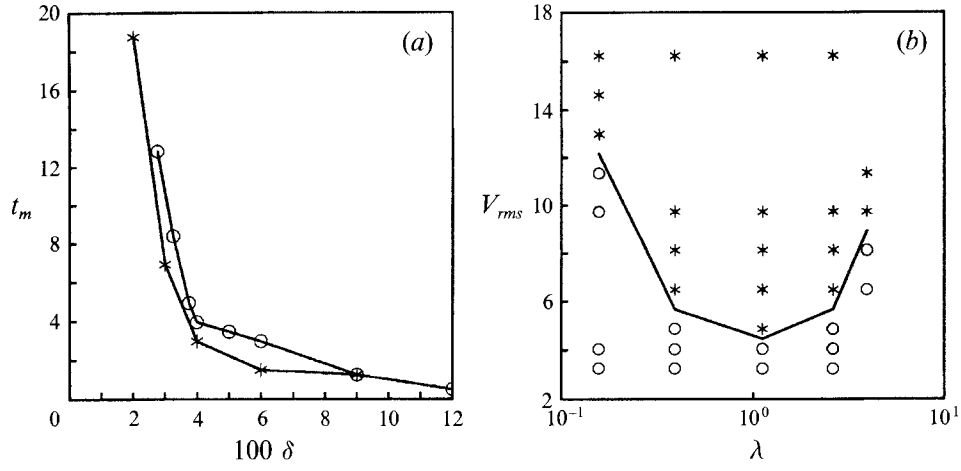

FIGURE 11. Stability plots for the triangle vortex. (*a*) The time to merger of two of the satellites for the perturbed triangle vortex as a function of the strength of the perturbation. The data points marked by asterisks (circles) correspond to the case in which the initial satellite vortex strengths are multiplied by $1+\delta$, $1-\delta$, $1(1+\delta, 1-\delta/2, 1-\delta/2)$. The merger time is expressed in units of the unperturbed vortex rotation period (81 s) and the perturbation strength in percent (i.e. 100δ). (*b*) The results from a stability study in which a random vorticity field of lengthscale λ and amplitude V_{rms} was added to the triangle vortex. Asterisks mark the experiments in which merger occurred between two of the three satellites before ten rotations periods of the unperturbed structure had elapsed. Circles mark those simulations in which the vortex system was still intact after ten rotation periods. The perturbation amplitude V_{rms} is given in multiples of the r.m.s. velocity of the triangle vortex, and λ is defined so that $\lambda = 1$ corresponds to the size of one side of the triangle vortex (see text).

In the second kind of stability study, we added a randomly generated homogeneous isotropic vorticity field to the vortex shown in figure 9. This perturbation field was created by adding contributions from all wavenumbers between two fixed limits, $k_0 \leqslant k_1$, in such a way that the energy spectrum of the perturbation was independent of wavenumber. The real and imaginary parts of the complex amplitude for each wavenumber were generated from a Gaussian distribution. In figure 11 (*b*) we show the resulting stability diagram. The perturbation amplitude is measured as the ratio of the r.m.s. velocity of the perturbation to the r.m.s. velocity of the triangular vortex. The r.m.s. averages are taken only over the area within an imaginary boundary of an idealized structure consisting of the triangle surrounded by three semicircles. The lengthscale of the perturbation is defined as $\lambda \equiv L_B/(L_\Delta \bar{k})$, where L_B is the size of the periodic computational box, $L_\Delta = 2a$ is the length of one side of the triangle vortex, and $\bar{k} = \frac{1}{2}(k_1 + k_0)$. Thus $\lambda = 1$ corresponds to the scale of the triangular vortex. The circles on this plot indicate the simulations in which the triangle vortex survives for more than ten rotation periods, and the asterisks indicate the simulations in which the triangle breaks up before that time limit is reached. Again the definition of a stability boundary is somewhat fuzzy. The fall off of time to merger for the points marked by asterisks is fairly steep as one moves away from the dark curve drawn in the diagram (just as in the case described by figure 11 *a*). Thus we see that the triangle vortex is most unstable to perturbations of lengthscale close to its own, and the minimum strength of the perturbation needed to destabilize it is about 3% measured in r.m.s. velocity. The structure appears very stable to large-scale perturbations, which for the most part simply advect it, and also to very small-scale perturbations, which are quickly sheared out to even smaller scales to be eventually dissipated by hyperviscosity.

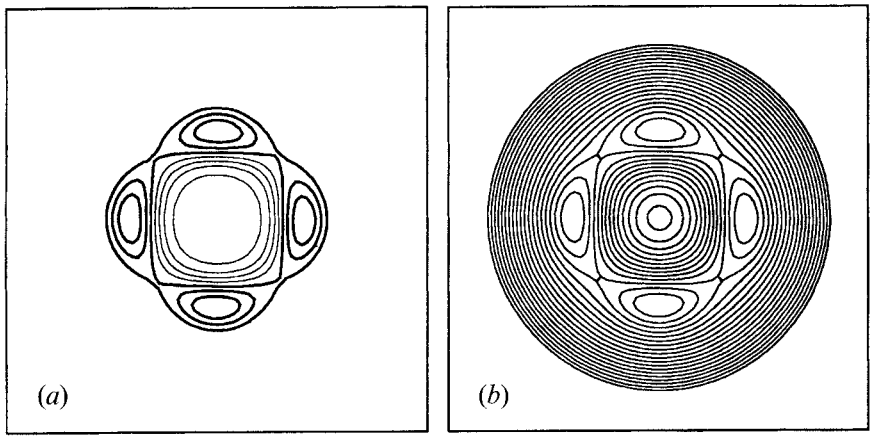

FIGURE 12. (*a*) Vorticity and (*b*) streamfunction contour plots of a square vortex. In (*a*) thick (thin) contours indicate positive (negative) relative vorticity; the contour level values are chosen to have increments of $\Delta\zeta = 0.3\ \mathrm{s}^{-1}$. The streamfunction shown in (*b*) is evaluated in the corotating frame with rotation period 44.8 s. Beyond a certain value, the high-level contours were not drawn because of 'bleeding' between the lines. The contour increment was taken as $\Delta\Psi = k^2\Delta\zeta$, where $ka = j_1^1$ and $a = 8.3$ cm is approximately the radius of the semicircular satellites. The dimensional velocity and length scales used in the initialization were $U = 20$ cm/s and $L = 11$ cm, and the length of a side of the computational domain was 90 cm (although here we have only plotted the field over an inner square of 54 cm on a side).

3.5 *Higher-order instabilities*

Seeing that the mode-3 instability leads through nonlinear saturation to the triangular vortex, we are led to investigate whether the mode-4 instability would lead to a square vortex. We performed a series of experiments with values of α running from 3 to 8, both with and without viscosity. To the unperturbed state we added a perturbation as defined by (5) with azimuthal mode number 4 only, with amplitudes varying from $\mu = 0.1$ to 0.5 and with lengthscale $\sigma = 1$ in the initial condition (2). Further exploration of the parameter space was not performed since we found that these somewhat arbitrary choices did lead to the formation of square vortices for $\alpha > 5$. The best-defined square vortices in our experiments formed for $\alpha = 7$ and 8. For example, in figure 12 we show the vorticity and streamfunction plots of a square vortex which formed for a steepness parameter of $\alpha = 8$. The simulation which produced this vortex was run with the molecular viscosity of water. The basic structure developed by time $t = 10$ s, and by $t = 72$ s the structure reached that shown in the figure. The vorticity pattern is shown in figure 12(*a*) and the streamfunction in the corotating frame of the vortex system is given in figure 12(*b*). The rotation rate of the structure was determined by inviscid simulation for one quarter of a rotation period. The scatter plot of the streamfunction and vorticity in the corotating frame is shown in figure 13. As with the triangle, the slope of the scatter plot in the positive vorticity range is well approximated by the proportionality constant which defines the Lamb dipole. The dashed line in the diagram results from taking $2a = 16.6$ cm as the length of one side of the square and then solving for k from $ka = j_1^1 \approx 3.83$. Unlike the triangle, however, the shape of the satellites here are somewhat narrower than semicircles with radius a. The thickness of the outer satellites is found to vary with the value of α.

In all the simulations in which the square vortex formed, the structure broke down before at most 3.5 rotations were completed. The inviscid runs preserved the structure the longest. The most long-lived square vortex was achieved for $\alpha = 8$, starting with a

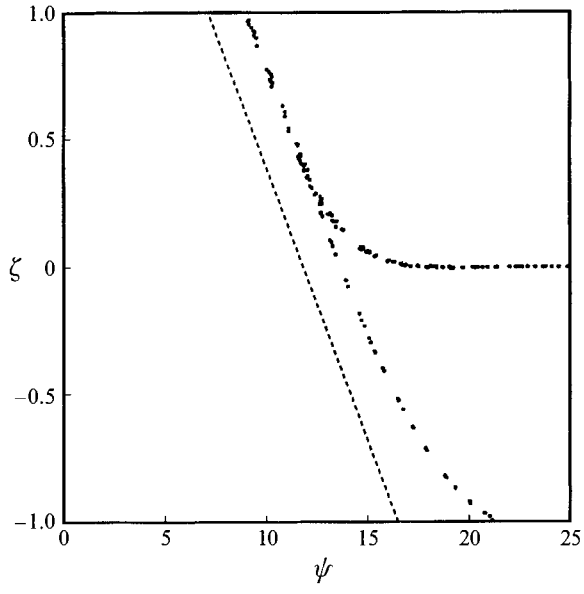

FIGURE 13. Scatter plot corresponding to the vorticity and streamfunction in the corotating frame that were shown in figure 12. In addition, the straight dashed line shows the slope in the relationship which defines the internal structure of the Lamb dipole: $\zeta = (ka)^2 \Psi$, where $ka = j_1^1$ and $a = 8.3$ cm is approximately one half of one side of the square.

perturbation amplitude of $\mu = 0.5$, with only hyperviscosity dissipation acting. In all cases, these square vortices, which have satellites of equal strength, broke down through the simultaneous merger of their satellites in two pairs on opposite sides of the square core. In order to assess the possibility of whether the square vortex could be observed in the rotating tank under the same conditions that produced the triangle vortex, we performed a simulation with the appropriate dissipation as discussed above (i.e. $T_E = 132$ s and $\nu = 0.01$ cm^2 s^{-1}). The initial vortex in this simulation was created with $\alpha = 8$, and a wavenumber-4 perturbation of amplitude $\mu = 0.125$. The resulting evolution is shown in figure 14. The square vortex formed after about 10 s. Unlike the triangle vortex which lasted indefinitely under the same conditions, this square vortex broke down after about two and a half rotations. The double satellite merger is shown in figure 14(*c*). This led to an intermediate tripole state (p*d*) which then broke down through the familiar double dipole instability. We also performed simulations in which the square vortex shown in figure 12 was perturbed by strengthening one satellite while correspondingly weakening another to preserve the total circulation. In those cases, only two satellites merged at first, leading to a temporary triangle vortex. Then another merger took place leading to the tripole state, and then finally the double dipole instability took over. From these results, we conclude that it should be possible to observe a square vortex emerge from a nearly circularly symmetric vortex in rotating-tank experiments if the initial perturbation is made sufficiently close to a pure mode-4 perturbation. However, it is also clear that it would only appear as a transitory state.

We have also been able to create a pentagon vortex in a numerical simulation by a wavenumber-5 perturbation on an $\alpha = 8$ profile. Although strong satellites do form rapidly, the structure breaks down after executing only about a half of a rotation. The breakdown began with the nearly simultaneous merger of two pairs of satellites which produced a roughly triangular system. Another merger followed, producing a tripole state. The tripole finally broke up into a dipole and monopole.

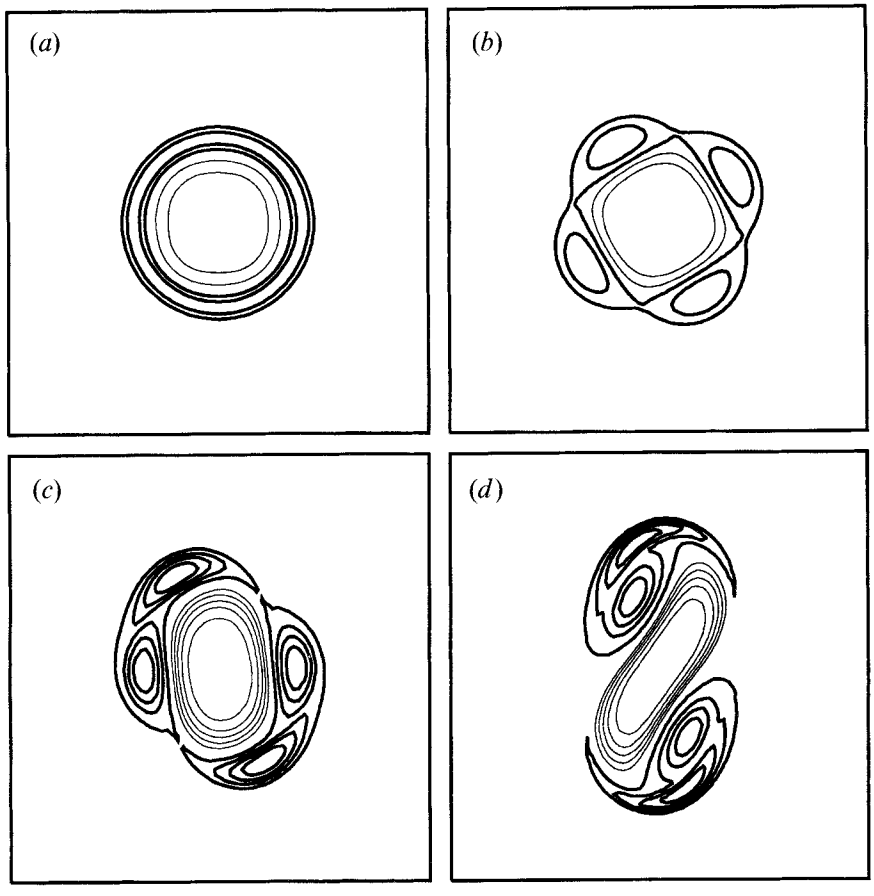

FIGURE 14. Vorticity contour plots showing the evolution of the square vortex. For this simulation we used a kinematic viscosity $\nu = 0.01$ cm^2 s^{-1} and bottom drag with an Ekman decay time of 132 s, thus demonstrating the possibility of producing a transitory square vortex in the rotating-tank under conditions similar to those in which the triangle was produced. The dimensional velocity and length scales used were $U = 20$ cm/s and $L = 11$ cm, and the length of a side of the computational domain was 90 cm. Thick (thin) lines represent positive (negative) contour levels. (*a*)–(*d*) Times $t = 0$, 80, 130 and 140 s, respectively, with contour-value increments of $\Delta\zeta = 0.8, 0.4, 0.12$ and 0.11 s^{-1}, respectively.

4. Point-vortex models

Further insight into the stability behaviour of the triangular vortex can be achieved through a consideration of a point-vortex model. The simplest model of the triangular vortex is obtained by replacing each of the three satellites by point vortices with circulations $\kappa_1, \kappa_2, \kappa_3$, each of the same sign, and the core vortex by a point vortex with circulation κ_4. Since we are only considering isolated vortices we have $\kappa_4 = -(\kappa_1+\kappa_2+\kappa_3)$. The equations are non-dimensionalized with lengthscale L, a typical distance between satellite and core, and time by $T = L^2/|\kappa|$, where κ is a typical circulation of one of the satellites.

If the satellites are slightly unequal a steadily rotating configuration can still be achieved, but the satellites will no longer be at the vertices of an equilateral triangle. For any combination of satellite strengths (within certain limits beyond which there are no steadily rotating triangular configurations) the positions of the satellites can be determined (see below), but there are no simple expressions for the positions or the rotation rate.

The equations of motion of a collection of point vortices can be derived from a Hamiltonian H (Batchelor 1967). They are (a dot denotes the time-derivative)

$$\kappa_i \dot{x}_i = \frac{\partial H}{\partial y_i}, \quad \kappa_i \dot{y}_i = -\frac{\partial H}{\partial x_i},$$

with

$$H = -\frac{1}{4\pi} \sum_{\alpha \neq \beta} \kappa_\alpha \kappa_\beta \log d_{\alpha\beta}. \tag{10}$$

Here $d_{\alpha\beta}$ is the Euclidean distance between vortex number α and vortex number β. Generally a system of four point vortices, unlike one with only two or three point vortices, is not integrable (cf. Aref & Pomphrey 1982). However, it has been noted by Eckhardt (1988) and Rott (1990) that in the case of zero net circulation and zero net impulse, there are enough integrals of motion in involution to reduce the effective number of degrees of freedom of the system to one. In this particular case a simple two-dimensional phase diagram contains all the information about the evolution of the system up to Galilean transformations (translations and rotations). The laboratory vortices as discussed in §2 are isolated and have no net impulse and thus the corresponding point-vortex model falls into the integrable class.

Following Eckhardt (1988), a canonical transformation is found in which the Hamiltonian, as given by (10), can be expressed as a function of two variables J and ϕ, with the distances given by the following expressions:

$$\left.\begin{aligned}
d_{12}^2 &= \frac{\kappa_4^2}{2\kappa_1(\kappa_2+\kappa_3)}\{(1+\rho^2)-(1-\rho^2)J+2\rho(1-J^2)^{\frac{1}{2}}\cos\phi\},\\
d_{34}^2 &= \frac{-\kappa_2\kappa_4}{2\kappa_3(\kappa_2+\kappa_3)}\{(1+\rho^2)+(1-\rho^2)J-2\rho(1-J^2)^{\frac{1}{2}}\cos\phi\},\\
d_{13}^2 &= \frac{\kappa_4^2}{2\kappa_1(\kappa_2+\kappa_3)}\{(1+\sigma^2)-(1-\sigma^2)J-2\sigma(1-J^2)^{\frac{1}{2}}\cos\phi\},\\
d_{24}^2 &= \frac{-\kappa_3\kappa_4}{2\kappa_2(\kappa_2+\kappa_3)}\{(1+\sigma^2)+(1-\sigma^2)J+2\sigma(1-J^2)^{\frac{1}{2}}\cos\phi\},\\
d_{14}^2 &= \frac{\kappa_2+\kappa_3}{2\kappa_1}(1-J),\\
d_{23}^2 &= \frac{-\kappa_4(\kappa_2+\kappa_3)}{2\kappa_2\kappa_3}(1+J),
\end{aligned}\right\} \tag{11}$$

where

$$\rho = (-\kappa_1\kappa_3/\kappa_2\kappa_4)^{\frac{1}{2}}, \quad \sigma = (-\kappa_1\kappa_2/\kappa_3\kappa_4)^{\frac{1}{2}}.$$

In Eckhardt (1988), the prefactors which explicitly depend on the circulations were not given. Since these prefactors are essential to the construction of the spatial configuration from given values of J and ϕ, and since their derivation is quite tedious and long, we give them here explicitly. Note that in our expressions the κ_i are signed and not, as in Eckhardt's notation, the absolute values of the circulations. In these non-dimensional expressions we have $J \in [-1, +1]$ and $\phi \in [0, \pi]$. To any pair (J, ϕ) there corresponds a unique configuration (up to the rotations and translations) of the four point vortices (with numbers 1–3 having positive circulation and number 4 with negative circulation) with zero net circulation and zero net impulse.

The evolution of the system modulo translations and rotations is along contours

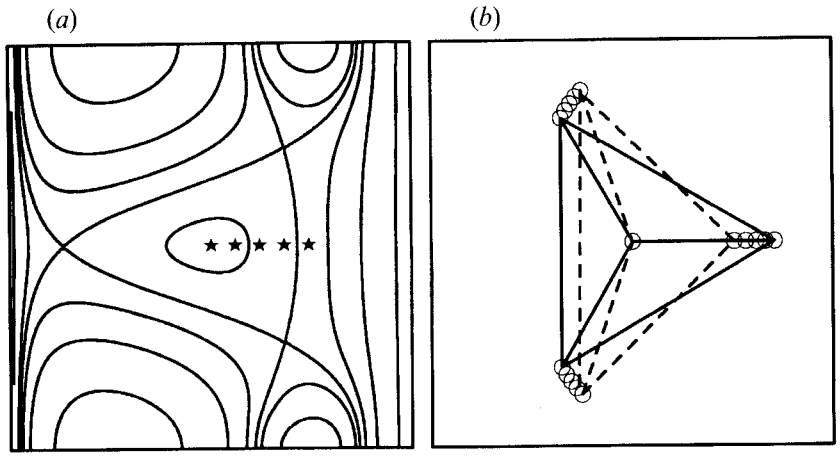

FIGURE 15. Diagrams illustrating the stability of the symmetric-strength four point-vortex system, under perturbations in shape. (*a*) A contour plot of the Hamiltonian for the four-point system with point-vortex strengths $\kappa_1 = \kappa_2 = \kappa_3 = 1$ and $\kappa_4 = -3$. J ranges from -1 to 1 on the horizontal axis, while ϕ ranges from 0 to π on the vertical. (*b*) The deformation of the shape of the four-point-vortex system corresponding to the phase-space coordinates J and ϕ indicated by the positions of the stars in (*a*). The solid lines in (*b*) indicate the shape of the fully symmetric configuration corresponding to the star at the extremum of the Hamiltonian at the centre of panel (*a*), and the dashed line shows the shape of the most perturbed configuration corresponding to the star outside the stable elliptical region in panel (*a*).

$H(J, \phi) =$ constant. The phase-space curves $H =$ constant for the symmetric case are shown in figure 15(*a*). In this case, i.e. $\kappa_1 = \kappa_2 = \kappa_3 = 1$ and $\kappa_4 = -3$, the steadily rotating configuration corresponds to $(J, \phi) = (0, \frac{1}{2}\pi)$. This is the elliptic fixed point in the middle of the phase diagram. Substitution of these values of J and ϕ in the above expressions for the $d_{\alpha\beta}$ verifies that the satellites are indeed at equal distances of magnitude 1 from the centre vortex and at the vertices of an equilateral triangle.

In general the values of J and ϕ for the steadily rotating state can be found by simultaneously solving

$$\frac{\partial H}{\partial J} = 0, \quad \frac{\partial H}{\partial \phi} = 0.$$

By substitution in the equations of motion the rotation rate can then be found. In the phase diagram there are six singularities where $|H| \to \infty$; these correspond to those situations where two point vortices come infinitesimally close. As is easily found with (11), they are at $J = \pm 1$ (the whole left and right boundaries of the diagram), and at $(J, \phi) = (J_\sigma, 0)$, $(J_\rho, 0)$, $(-J_\sigma, \pi)$ and $(-J_\rho, \pi)$, where $J_\sigma = (1-\sigma^2)/(1+\sigma^2)$ and $J_\rho = (\rho^2-1)/(\rho^2+1)$.

From figure 15(*a*) it is clear that the symmetric steadily rotating configuration is stable to sufficiently small perturbations of the positions of the satellites. If perturbed enough, the system is placed on one of the phase curves that extend away from the fixed point. To see how much of a perturbation is needed to put the configuration on a phase curve that does not enclose the fixed point, we have drawn a number of stars in figure 15(*a*) starting at the elliptic point outwards along the line $\phi = \frac{1}{2}\pi$. In figure 15(*b*) we have drawn the physical configurations corresponding to the (J, ϕ) values marked by stars in figure 15(*a*). The configuration marked by the star just inside the stable region corresponds approximately to a 20% variation in the distance of one of the satellites from the centre point. The value for J needed for a perturbation of a given size is

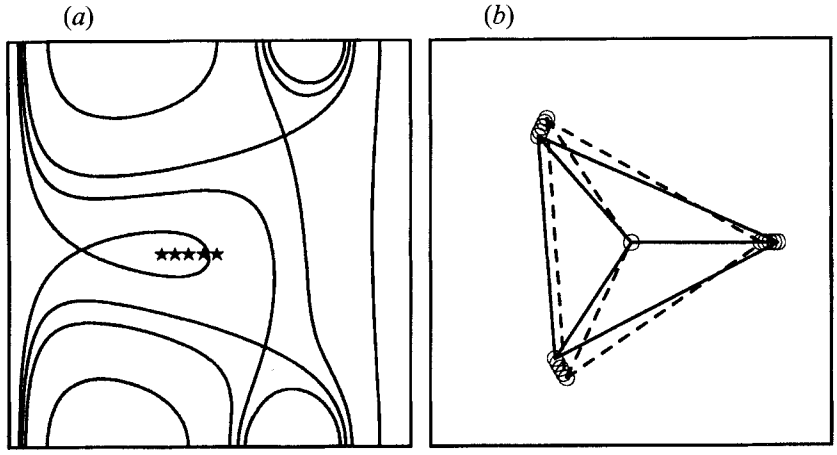

FIGURE 16. As figure 15 but for $\kappa_1 = 1.1$, $\kappa_2 = 0.9933$, $\kappa_3 = 0.9067$, $\kappa_4 = -3.0$.

readily computed from (11) for d_{14} (e.g. for $d_{14} = 0.8$, $J = 0.36$ and then keeping $\phi = \frac{1}{2}\pi$ the rest of the of the distances can be computed easily). The configuration indicated by the star outside the closed elliptic region in figure 15(*a*) is unstable. This state corresponds to a perturbation of almost 30% in the distance d_{14} from the symmetric case at $J = 0$. The spatial configuration corresponding to this unstable initial condition is indicated by the dashed line in figure 15(*b*). In this case, in less than one rotation period, one of the satellites overtakes the one ahead of it and moves in between it and the core vortex, and this corresponds to moving up or down along the vertically oriented lines on the right-hand side of the elliptic region in figure 15(*a*). This is also what happens just before the merger of two of the satellites in our examples of the instability of the triangle with continuous vorticity fields. By comparing the dashed triangle with the solid triangle (the steadily rotating configuration), one can see how strong the initial perturbation must be for instability. Perturbations in other directions away from the centre in figure 15(*a*) correspond to even stronger deformations.

Considerably less of a perturbation is needed, though, to make the steadily rotating configuration unstable when the satellites have unequal strengths. As was shown by Eckhardt (1988), the closed region around the elliptic fixed point shrinks in size when the strengths of the satellites are made unequal. With a 10% variation in the strength of the satellites, the spatially symmetric configuration is no longer stable. We show this in figure 16 with the aid of the phase diagram for the particular case $\kappa_1 = 1.1$, $\kappa_2 = 0.9933$, $\kappa_3 = 0.9067$, $\kappa_4 = -3.0$ which was previously treated by Eckhardt (1988). Again we have indicated a number of positions on the phase diagram (figure 16*a*) and constructed their corresponding spatial configurations (figure 16*b*). Note that the stable configuration (solid lines) corresponding to the elliptic fixed point is not spatially symmetric. On the other hand, the nearly symmetric configuration (dashed lines) is unstable and lies on a trajectory that takes it towards the left border of the phase diagram, which corresponds to the singular point $d_{23} = 0$. In this case two of the satellites will eventually come very close. For even larger differences between the strengths of the satellites, the size of the closed region around the fixed point shrinks to zero (see Eckhardt 1988) and there is no longer a steadily rotating triangular configuration. The main conclusion is that the steadily rotating triangular vortex model is (nonlinearly) stable to small enough perturbations, but with a stability domain that decreases rapidly in size when the strengths of the satellites become unequal.

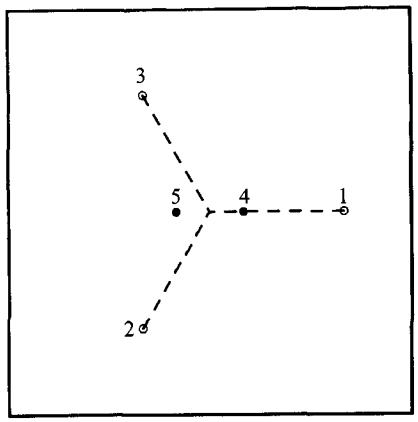

FIGURE 17. Diagram showing the positions of the positive vortices (open circles) representing the satellites and the negative vortices (filled circles) representing the extended core in the five-point-vortex model of the triangle vortex. The distance between the negative vortices is $d = 0.5$.

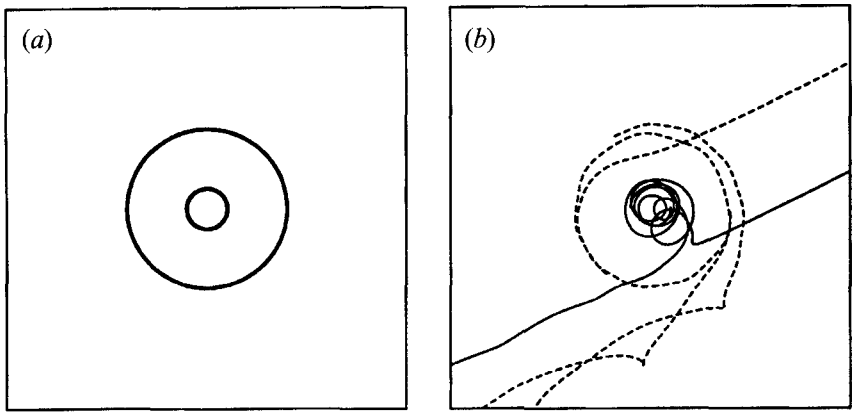

FIGURE 18. Diagram showing the trajectories of the vortices for the five-point model shown in figure 17 with two different sets of vortex strengths. (*a*) The strengths are given by $\kappa_1 = \kappa_2 = \kappa_3 = 1$ and $\kappa_4 = \kappa_5 = -1.5$. These trajectories illustrate that splitting the core vortex alone does not destabilize the system. (*b*) The strengths have been altered according to (12) with the perturbation parameter given by $\delta = 12.5\%$.

As an interesting aside, we note that by giving some structure to the core by representing it by two point vortices instead of one, we can capture the essential features of the entire instability scenario. The configuration of the five-point model is drawn in figure 17. We fix the sum of the strengths of the satellites at 3 and the sum of the strengths of the core anticyclones at -3. The case in which d, the distance between the anticyclones, is zero is equivalent to the four-point model. First of all, we consider the symmetric case with $\kappa_1 = \kappa_2 = \kappa_3 = 1$ and $\kappa_4 = \kappa_5 = -1.5$. For choices of d less than 0.78, we found that the orbits of the point vortices are all nearly circular, or, more precisely, the satellites remain in orbits bounded by two circles of radii near $r = 1$ while the two core vortices remain in orbits bounded by two circles of radii near $\frac{1}{2}d$. For example, figure 18(*a*) shows the orbits, for a period of four revolutions of the outer vortices, for the case with $d = 0.5$. Thus, for a large range of values of d, this is also a good model for a symmetric triangle vortex.

Through numerical simulations we examined the results of changes in strengths while leaving the initial positions as shown in figure 17 (with $d = 0.5$). For simplicity

we chose to examine only the case in which one satellite is made stronger at the equal expense of the other two. The constraints of zero total circulation and zero momentum then fix the values of the interior vortices. Thus we take

$$\kappa_1 = 1+\delta, \quad \kappa_2 = 1-\tfrac{1}{2}\delta, \quad \kappa_3 = 1-\tfrac{1}{2}\delta, \tag{12}$$

and

$$\kappa_4 = -\tfrac{3}{2}-3\delta, \quad \kappa_5 = -\tfrac{3}{2}+3\delta,$$

where δ is arbitrary. For $0.124 \leqslant \delta \leqslant 0.133$, the evolution captures most of the important features observed in the laboratory experiments. For δ somewhat less that 0.124 the configuration does not split, and for δ somewhat larger than 0.133 a wide variety of behaviour is observed. The exact boundaries of the range of δ for which the behaviour is as in the laboratory experiments is difficult to determine due to the sensitivity of the results to initial data and numerical error near these boundaries. Figure 18(*b*) shows the orbits of the five points for the case $\delta = 0.125$, with solid (dashed) curves indicating the trajectories of the satellites (core vortices). After approximately three-quarters of an orbit the strongest of the satellites pairs with the weaker of the two core vortices, forming a dipole which leaves the figure at the right. Meanwhile, the two weaker satellites begin to rotate around each other and as a unit combine with the strong core vortex to form a dipole structure which propagates off to the left in the figure. This mutual orbiting of the two weak cyclones is observed in the laboratory experiment as a prelude to the merger of these vortices into a single cyclone (see figure 2). Of course, with the point vortices this merger cannot actually occur (unless some *ad hoc* rule were appended to the dynamics as in Carnevale *et al.* 1991). However, the fact that the three-point structure that moves off to the left continues to act essentially as a dipole is sufficient for our current purpose.

Finally, we turn to the stability of the higher-order geometrical vortices, the square, the pentagon, etc., from the point of view of point-vortex models. Specifically, we consider here only the zero-circulation steadily rotating configurations consisting of n equal-strength point vortices symmetrically placed on a circle centred on a point vortex of opposite sign. It can be shown that the case $n = 2$, a model for the tripole, is nonlinearly stable (Kloosterziel 1990), and we have seen above that Eckhardt's (1988) analysis proves that the case $n = 3$, the model of the triangular vortex, is also nonlinear stable (cf. figure 15*a*). Morikawa & Swenson (1971) performed a linear stability analysis on these models for all n. The perturbations they considered were small displacements in the initial positions. Consistent with the later nonlinear stability results, they found that the cases $n = 2$ and 3 are linearly stable, but more importantly, they proved that for all cases $n \geqslant 4$ the configurations are linearly unstable. We illustrate this instability for the cases $n = 4$ and 5, the models of the square and pentagon vortices, in figure 19. For these fully nonlinear simulations of the evolution, initial perturbations were made only in the initial positions of the satellites. In each case, one satellite was moved 1% further away from the centre vortex, and the other satellite positions were perturbed to a lesser extent but in such a way that the net momentum of the complete structure remained zero as in the unperturbed case. Figure 19 shows that in less than one rotation, the trajectories deviate greatly from the circle, and that the system reaches the stage where at least one of the satellites has caught up with the one ahead of it in angular position and has moved in between it and the centre vortex. This is the same form of instability that led to the close approach and merger of satellites in our simulations of the continuous square and pentagon vortices. This should be contrasted with the case of the point-vortex model of the triangle, where we saw that perturbations of even 20% in the positions of the satellites can still be stable.

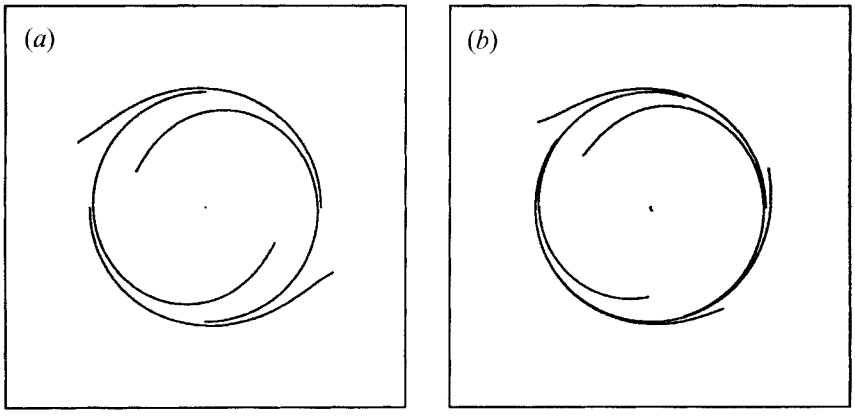

FIGURE 19. Diagram showing the instability in the trajectories of the vortices for the five- and six-point models of the square and pentagon vortices. In the unperturbed cases, the satellites lie on a circle centred on the core vortex. Here the satellites are initially perturbed from those positions by at most 1%. The figure shows the perturbed orbits up to the point where at least one of the satellites moves in between the one ahead of it and the core vortex.

In view of the results of Morikawa & Swenson (1971), we anticipate that all higher-order coherent vortices that may form through amplification of wavenumbers even higher than 5 are also unstable.

5. Summary

Inspired by laboratory observations, we have investigated the emergence and evolution of triangular vortices and higher-order geometrical vortices through numerical simulations. We have shown that it is possible to create a stable symmetrical triangle vortex from a circularly symmetric profile by a pure mode-3 instability. This triangle vortex was shown to be stable to perturbations of amplitude less than about 3% in either velocity or vorticity amplitude. In the parameter regime where the pure wavenumber-3 instability yields the triangle vortex, the growth rates of neighbouring wavenumbers are all of the same order of magnitude. It is for this reason that arbitrary initial perturbations containing all these components in their spectrum lead to the formation of asymmetric unstable triangular vortices. This is typically the case in the laboratory, and usually the triangular vortex is observed to change into a tripole, through the merger of two satellites, and subsequently break up into either two dipoles or a dipole plus monopole. These observations have been compared to predictions based on point-vortex models in §4. The point-vortex model of the symmetric triangular vortex is stable to finite perturbations of both the equilibrium positions and the strengths of the satellites. If the satellites are sufficiently asymmetric in strength (e.g. 10% variation) and placed symmetrically about the core vortex, then the structure is highly unstable. The instability leads to the close approach of two of the satellites, which in the continuous system leads to merger. The events observed in the laboratory and in the simulations can be captured by the point-vortex model if the core is replaced by two point vortices. The instability then proceeds with dipole splitting.

The higher-order geometrical vortices that we examined, the square and the pentagon, proved unstable even when symmetrically prepared. Furthermore, the results of Morikawa & Swenson (1971) concerning the stability of point-vortex models for the higher-order structures suggest that the triangle vortex is probably the only stable member of the family of geometrical vortices. Thus, the set of stable coherent by-

products of the breakup of simple unstable circularly symmetric isolated vortices of the type considered here most likely only includes the monopole, dipole, tripole and triangle vortices.

After the submission of our original manuscript, we discovered that another study of geometrical vortices was performed by G. Morel and X. J. Carton but not published (SHOM internal report on oceanography 1991). They used contour dynamics to study the stability of these vortices with piecewise-constant vorticity from triangles up to and including octagons and reached the same conclusion that we did, namely that only the triangle is stable. Also since this manuscript was first submitted, an article has appeared on instabilities of tornados (Lin 1992) which shows, with contour dynamics, the instability of a circularly symmetric vortex leading to the triangle vortex.

This research has been supported in part by National Science Foundation grant OCE 91-21998 and Office of Naval Research grant N00014-93-1-0459. The numerical simulations were performed at the San Diego Super Computer Center. The laboratory experiments were performed in the Applied Mechanics and Engineering Sciences department at University of California, San Diego. We are grateful for some very helpful comments by the referees.

REFERENCES

AREF, H. & POMPHREY, N. 1982 Integrable and chaotic motions of four vortices. I. The case of identical vortices. *Proc. R. Soc. Lond.* A **380**, 359–387.

BATCHELOR, G. K. 1967 *An Introduction to Fluid Dynamics*. Cambridge University Press.

CARNEVALE, G. F., BRISCOLINI, M., PURINI, R. & VALLIS, G. K. 1988 Numerical experiments on modon stability to topographic perturbations. *Phys. Fluids* **31**, 2562–2566.

CARNEVALE, G. F., MCWILLIAMS, J. C., POMEAU, Y., WEISS, J. B. & YOUNG, W. R. 1991 Evolution of vortex statistics in two-dimensional turbulence. *Phys. Rev. Lett.* **64**, 2735–2737.

CARTON, X. J., FLIERL, G. R. & POLVANI, L. M. 1989 The generation of tripoles from unstable axisymmetric isolated vortex structures. *Europhys. Lett.* **9**, 339–344.

CARTON, X. J. & MCWILLIAMS, J. C. 1989 Barotropic and baroclinic instabilities of axisymmetric vortices in a quasi-geostrophic model. In *Mesoscale/Synoptic Coherent Structures in Geophysical Turbulence* (ed. J. C. J. Nihoul & B. M. Jamart), pp. 225–244. Elsevier.

ECKHART, B. 1988 Integrable four vortex motion. *Phys. Fluids* **31**, 2796–2801.

FLIERL, G. R. 1988 On the instability of geostrophic vortices. *J. Fluid Mech.* **197**, 349–388.

GENT, P. R. & MCWILLIAMS, J. C. 1986 The instability of circular vortices. *Geophys. Astrophys. Fluid Dyn.* **35**, 209–233.

GREENSPAN, H. P. 1968 *The Theory of Rotating Fluids*. Cambridge University Press.

HEIJST, G. J. F. VAN & KLOOSTERZIEL, R. C. 1989 Tripolar vortices in a rotating fluid. *Nature, Lond.* **338**, 569–571.

HEIJST, G. J. F. VAN, KLOOSTERZIEL, R. C. & WILLIAMS, C. W. M. 1991 Laboratory experiments on the tripolar vortex in a rotating fluid. *J. Fluid Mech.* **225**, 301–322.

KLOOSTERZIEL, R. C. 1990 Barotropic vortices in a rotating fluid. PhD thesis, University of Utrecht, The Netherlands.

KLOOSTERZIEL, R. C. & HEIJST, G. J. F. VAN 1991 An experimental study of unstable barotropic vortices in a rotating fluid. *J. Fluid Mech.* **223**, 1–24.

LAMB, H. 1932 *Hydrodynamics*. Cambridge University Press.

LEGRAS, B., SANTANGELO, P. & BENZI, R. 1988 High-resolution numerical experiments for forced two-dimensional turbulence. *Europhys. Lett.* **5**, 37–42.

LIN, S.-J. 1992 Contour dynamics of tornado-like vortices. *J. Atmos. Sci.* **49**, 1745–1756.

MORIKAWA, G. K. & SWENSON, E. V. 1971 Interacting motion of rectilinear geostrophic vortices. *Phys. Fluids* **14**, 1058–1073.

NGUYEN DUC, J. M. & SOMMERIA, J. 1988 Experimental characterization of steady two-dimensional vortex couples. *J. Fluid Mech.* **192**, 175–192.

ORLANDI, P. & HEIJST, G. J. F. VAN 1992 Numerical simulation of tripolar vortices in 2D flow. *Fluid Dyn. Res.* **9**, 170–206.

PATTERSON, G. S. & ORSZAG, S. A. 1972 Spectral calculations of isotropic turbulence, efficient removal of aliasing interactions. *Phys. Fluids* **14**, 2538–2541.

ROTT, N. 1990 Constrained three- and four-vortex problems. *Phys. Fluids* A **2**, 1477–1480.